ARMY RESEARCH LABORATORY

ARL

Guidance and Control of a Man-Portable Precision Munition Concept

by Frank Fresconi and Jon Rogers

NOTICES

Disclaimers

The findings in this report are not to be construed as an official Department of the Army position unless so designated by other authorized documents.

Citation of manufacturer's or trade names does not constitute an official endorsement or approval of the use thereof.

Destroy this report when it is no longer needed. Do not return it to the originator.

Army Research Laboratory

Aberdeen Proving Ground, MD 21005-5066

Guidance and Control of a Man-Portable Precision Munition Concept

Frank Fresconi
Weapons and Materials Research Directorate, ARL

Jon Rogers
Georgia Institute of Technology

REPORT DOCUMENTATION PAGE		*Form Approved* *OMB No. 0704-0188*
Public reporting burden for this collection of information is estimated to average 1 hour per response, including the time for reviewing instructions, searching existing data sources, gathering and maintaining the data needed, and completing and reviewing the collection information. Send comments regarding this burden estimate or any other aspect of this collection of information, including suggestions for reducing the burden, to Department of Defense, Washington Headquarters Services, Directorate for Information Operations and Reports (0704-0188), 1215 Jefferson Davis Highway, Suite 1204, Arlington, VA 22202-4302. Respondents should be aware that notwithstanding any other provision of law, no person shall be subject to any penalty for failing to comply with a collection of information if it does not display a currently valid OMB control number. **PLEASE DO NOT RETURN YOUR FORM TO THE ABOVE ADDRESS.**		

1. REPORT DATE *(DD-MM-YYYY)*	2. REPORT TYPE	3. DATES COVERED (From - To)
June 2014	Final	1 October 2013–28 February 2014

4. TITLE AND SUBTITLE	5a. CONTRACT NUMBER
Guidance and Control of a Man-Portable Precision Munition Concept	
	5b. GRANT NUMBER
	5c. PROGRAM ELEMENT NUMBER

6. AUTHOR(S)	5d. PROJECT NUMBER
Frank Fresconi and Jon Rogers	AH43
	5e. TASK NUMBER
	5f. WORK UNIT NUMBER

7. PERFORMING ORGANIZATION NAME(S) AND ADDRESS(ES)	8. PERFORMING ORGANIZATION REPORT NUMBER
U.S. Army Research Laboratory ATTN: RDRL-WML-E Aberdeen Proving Ground, MD 21005-5066	ARL-TR-6966

9. SPONSORING/MONITORING AGENCY NAME(S) AND ADDRESS(ES)	10. SPONSOR/MONITOR'S ACRONYM(S)
	11. SPONSOR/MONITOR'S REPORT NUMBER(S)

12. DISTRIBUTION/AVAILABILITY STATEMENT

Approved for public release; distribution is unlimited.

13. SUPPLEMENTARY NOTES

14. ABSTRACT

The hypothesis of this report is that delivery accuracy of small-diameter spin-stabilized projectiles can be improved through novel guidance and control techniques using low-cost components. A gyroscopically stable projectile equipped with a strap-down detector and rotary actuation assembly is introduced. Flight models are formulated to enable nonlinear simulation. The unique guidance challenges posed by characteristics of spin-stabilized flight dynamics such as limit cycles, center-of-gravity swerve, instability, and practical feedback are illustrated. New guidance and control techniques to circumvent these difficulties are proposed. Modeling, parameter estimation, and stability analysis results underpin control design. Representative feedback, control commands, and flight behaviors from nonlinear simulations demonstrate the efficacy of this guidance approach. Monte Carlo analysis shows more than a factor of two in accuracy improvement of the guided over the ballistic flight. These results indicate that delivery system improvements are achievable in small, gyroscopically stable projectiles containing low-cost guidance elements using integrated control formulations.

15. SUBJECT TERMS

guidance, flight control, spin stabilized, airframe, infantry squad weapons

16. SECURITY CLASSIFICATION OF:			17. LIMITATION OF ABSTRACT	18. NUMBER OF PAGES	19a. NAME OF RESPONSIBLE PERSON Frank Fresconi
a. REPORT	b. ABSTRACT	c. THIS PAGE			19b. TELEPHONE NUMBER *(Include area code)*
Unclassified	Unclassified	Unclassified	UU	40	(410) 306-0794

Contents

List of Figures

List of Tables

Acknowledgments

1. Introduction

The motivation for this study is to enhance the lethality of the infantry squad though precision guidance technologies for small-diameter projectiles. Assault and carbine rifles, grenade launchers, and machine guns have been the backbone of the infantry for many years. Application of miniaturized low-cost sensors and actuators to projectiles in this environment features the potential to revolutionize squad-level lethal capability.

Precision guidance implies some means of navigating and maneuvering the lethal payload. The global positioning system (GPS) (*1*, *2*), inertial measurement units (*3*), and seekers (*4*) often navigate munitions to the target. Course correction may be achieved through aerodynamic (*5*) or jet (*6*) control. These technologies are adversely affected by constraints for squad-level weapons. Volume is a critical concern since the diameter of these projectiles ranges from 5.56 to 40 mm. These projectiles are launched from rifled guns that produce spin rates of hundreds to thousands of rotations per second. The nonlinear dynamics of high-spin-rate projectiles complicates the sensor stimuli and stresses the actuator bandwidth. Precision guidance technologies in most squad-level weapons must perform quickly because the time of flight is often only a few seconds. It is essential that these technologies be low cost and easy to use for proliferation on the battlefield.

The hypothesis of this study is that flight control algorithms and novel system concepts using low-cost sensor and actuator components can effectively guide small-diameter gyroscopically stabilized projectiles. Guidance and flight control techniques for large, slowly rolling projectiles (*1*, *7–9*) exist in the literature, but there is no published work for small, fast-spinning airframes. These flight bodies exhibit unique characteristics that increase the difficulty of the guidance problem. A simple strap-down detector (*4*) supplies the only feedback in this report. Strap-down detectors, as opposed to gimbaled systems, are rigidly mounted to the projectile. The maneuver mechanism is an innovative configuration using gun-hardened commercial-off-the-shelf motors to rotate miniature wings into the airstream (*10–13*).

This report introduces the guided projectile concept. Flight models are provided for subsequent implementation in simulation. Some representative flight behaviors, which complicate the guidance problem and preclude traditional solutions, are provided. A reference-following-based guidance and control approach is outlined. System identification, parameter estimation, stability, and control algorithms are presented. Notional ballistic and controlled flight simulation results are given along with Monte Carlo system simulations that demonstrated the efficacy of these techniques. A nomenclature of terms and calculations is provided at the end of this report.

2.   Concept

The guidance and control of the present work applies to the gamut of squad weapons. A rendering of the projectile with the maneuver and navigation technologies is shown in figure 1. A 40-mm-diameter projectile is used throughout this report as an illustrative example. The 40-mm grenade system features a subsonic launch and a projectile spin rate of approximately 60 Hz.
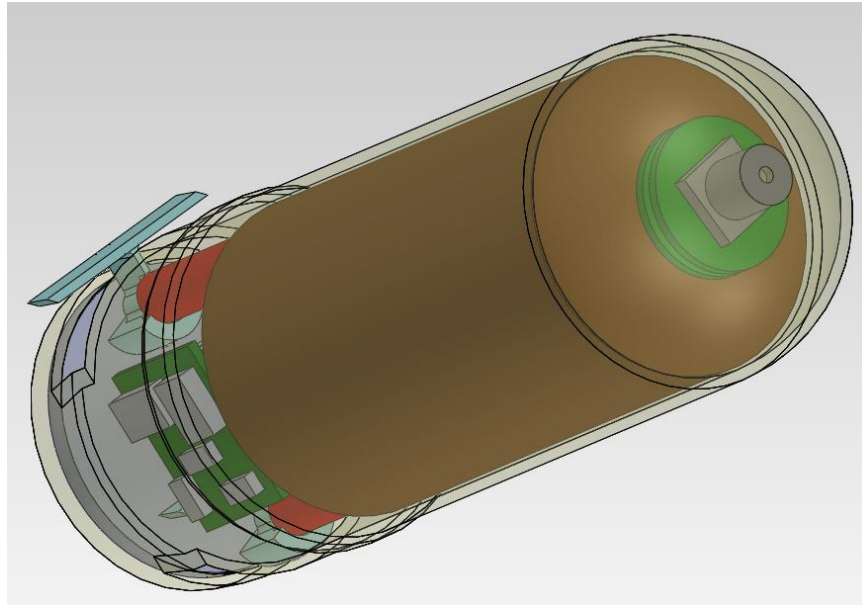

Figure 1. Spin-stabilized projectile with navigation and maneuver components.

To reduce cost and ensure survivability during gun launch, commercial optic, imager, and supporting electronic components are packaged in a strap-down manner at the nose. Effective usage of wider field-of-view lenses balanced with sufficient control authority for given ballistic launch, and flight uncertainties ensure that once the designated spot is detected on the imager, the lethal payload can be maneuvered close to the target. Fuzing and warhead are contained in the central portion of the projectile body.

The maneuver mechanism is placed at the aft end of the spin-stabilized projectile to maximize control authority (*14, 15*). The maneuver section includes power conditioning electronics, processor, microelectromechanical inertial sensors, battery, and the actuator. This mechanism consists of a rotary motor (red in figure 1) linked to a deflected wing (light blue in figure 1). As the projectile body spins over one revolution, the motor rotates the wing in the opposite direction at the same rate. This deploys the wing into the airstream for a portion of the roll cycle to create an aerodynamic asymmetry. An assortment of means may be used to vary the control effort since the wing has a fixed deflection angle. Control commands can "fishtail" the flight, a clutch can decouple the motor and wing, the wings can rotate at a frequency off the projectile spin rate, or

multiple motor-wing assemblies can mix the relative phasing of roll angle to deploy the wings into the airstream. For the purposes of this study, two motor-wing assemblies were packaged near the projectile base oriented 180° apart in roll angle. See Fresconi et al. (*10*), Fresconi et al. (*11*), Gross et al. (*12*), and Fresconi et al. (*13*) for more details.

The design of maneuvering spin-stabilized airframes is an active research area. Large control authority is difficult to obtain due to gun-launched packaging constraints and because dynamic flight instabilities (*16, 17*) often arise. Further difficulties result in the present investigation because the flight is subsonic and little dynamic pressure is available. Other maneuver mechanisms available in the literature for small-diameter spin-stabilized projectiles use flow (*18–20*) or jet (*21*) control techniques.

3. Flight Modeling

To study the flight of this guided projectile concept, models of the aerodynamics, flight mechanics, actuator, and feedback measurements must be formulated and implemented in simulation. The body-fixed coordinate system, illustrated in figure 2, defines the aerodynamic angles and forces and moments.
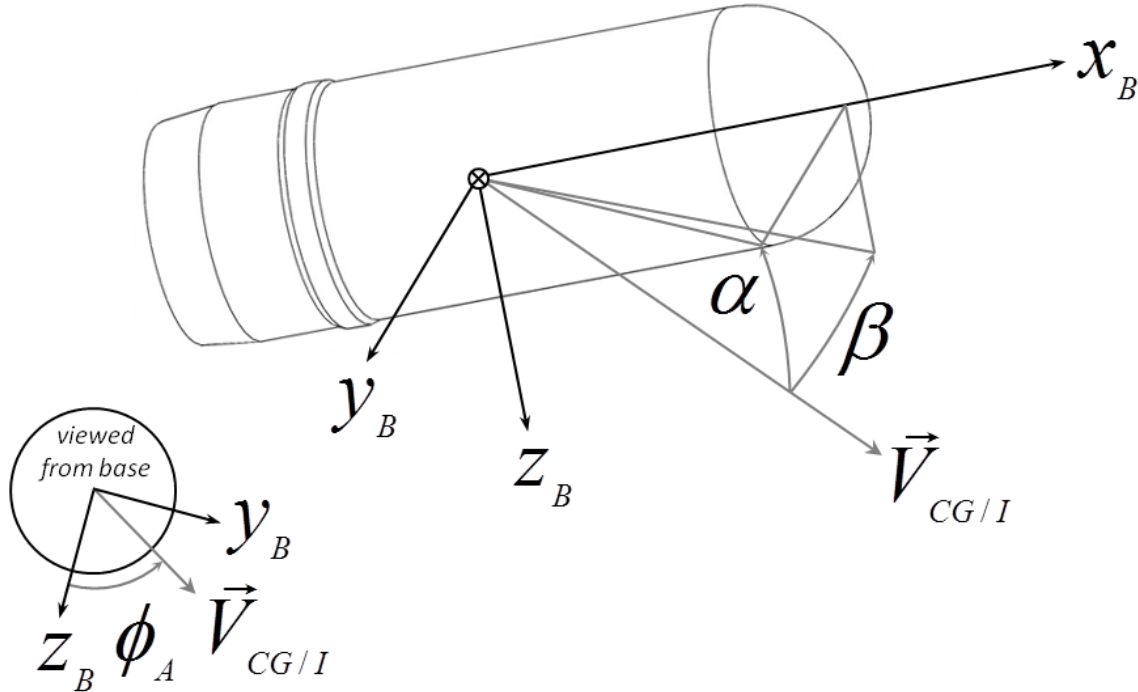

Figure 2. Body-fixed coordinate system.

Aerodynamic forces and moments consist of rigid (projectile body) and moveable (wing) surfaces.

$$
\begin{aligned}
X &= X^R + X^M \\
Y &= Y^R + Y^M \\
Z &= Z^R + Z^M
\end{aligned}
\tag{1}
$$

$$
\begin{aligned}
L &= L^R + L^M \\
M &= M^R + M^M \\
N &= N^R + N^M
\end{aligned}
\tag{2}
$$

Projectile body (rigid) forces include axial force, normal force, and side (Magnus) force.

$$
\begin{aligned}
X^R &= -qS\left[C_{X_0}(M) + C_{X_{\alpha^2}}(M)\bar{\alpha}^2\right] \\
Y^R &= -qS\left[C_{N_\alpha}(M)\beta + C_{N_{\alpha^3}}(M)\beta^3 - C_{Y_{p\alpha}}(M,\bar{\alpha})\alpha\frac{pD}{2V}\right] \\
Z^R &= -qS\left[C_{N_\alpha}(M)\alpha + C_{N_{\alpha^3}}(M)\alpha^3 + C_{Y_{p\alpha}}(M,\bar{\alpha})\beta\frac{pD}{2V}\right]
\end{aligned}
\tag{3}
$$

Projectile body (rigid) moments include roll damping, static pitching, pitch damping, and Magnus components.

$$
\begin{aligned}
L^R &= qSD\left[C_{l_p}(M)\frac{pD}{2V}\right] \\
M^R &= qS\left[C_{m_\alpha}(M)\alpha + C_{m_{\alpha^3}}(M)\alpha^3 + C_{m_q}(M)\frac{qD}{2V} + C_{n_{p\alpha}}(M,\bar{\alpha})\beta\frac{pD}{2V}\right] \\
N^R &= qS\left[-C_{m_\alpha}(M)\beta - C_{m_{\alpha^3}}(M)\beta^3 + C_{m_q}(M)\frac{rD}{2V} + C_{n_{p\alpha}}(M,\bar{\alpha})\alpha\frac{pD}{2V}\right]
\end{aligned}
\tag{4}
$$

A general model of the wing aerodynamic forces and moments was built. Some relevant roll angles are defined because the wing aerodynamics depend on these states. The relative roll angle of the wing follows:

$$
\Phi_i = \phi_{C_i} - \phi
\tag{5}
$$

The amount of wing exposed to the airstream is tracked through a stowed roll angle.

$$
\hat{\phi}_i = \Phi_i - \phi_{B_i}
\tag{6}
$$

The total ($\bar{\alpha}_{M_i}$) and yaw (β_{M_i}) angles of attack of the wing also need to be computed to determine the wing aerodynamics.

$$
\bar{\alpha}_{M_i} = asin\left(\frac{\sqrt{v_{M_i}^2 + w_{M_i}^2}}{\sqrt{u_{M_i}^2 + v_{M_i}^2 + w_{M_i}^2}}\right)
\tag{7}
$$

$$\beta_{M_i} = asin\left(\frac{v_{M_i}}{\sqrt{u_{M_i}{}^2 + v_{M_i}{}^2 + w_{M_i}{}^2}}\right) \tag{8}$$

The local velocity at each wing in local wing coordinates is obtained through the following expression.

$$[u_{M_i} \quad v_{M_i} \quad w_{M_i}]^T = \vec{T}_{BM_i}(\vec{V}_{CG/I} + \vec{\omega}_{B/I} \times \vec{r}_{CG \to CP_i}) \tag{9}$$

The aerodynamic coefficients for each wing are calculated using polynomial expansions. The relationship between the aerodynamics and the amount of the wing exposed to the airstream is embedded through the dependence on the stowed roll angle.

$$C_X^{M_i} = C_{X_0}^M(M, \hat{\phi}_i) + C_{X_{\alpha_M}}^M(M, \hat{\phi}_i)\beta_{M_i} + C_{X_{\alpha^2_M}}^M(M, \hat{\phi}_i)\beta_{M_i}^2 + C_{X_{\alpha^3_M}}^M(M, \hat{\phi}_i)\beta_{M_i}^3$$

$$C_Z^{M_i} = C_{Z_0}^M(M, \hat{\phi}_i) + C_{Z_{\alpha_M}}^M(M, \hat{\phi}_i)\beta_{M_i} + C_{Z_{\alpha^3_M}}^M(M, \hat{\phi}_i)\beta_{M_i}^3$$

$$C_l^{M_i} = C_{l_0}^M(M, \hat{\phi}_i) + C_{l_{\alpha_M}}^M(M, \hat{\phi}_i)\bar{\alpha}_{M_i} \tag{10}$$

$$C_m^{M_i} = C_{m_0}^M(M, \hat{\phi}_i) + C_{m_{\alpha_M}}^M(M, \hat{\phi}_i)\beta_{M_i} + C_{m_{\alpha^3_M}}^M(M, \hat{\phi}_i)\beta_{M_i}^3$$

Equations for the aerodynamic forces and moments of each wing in projectile body coordinates are provided.

$$\begin{bmatrix} X^{M_i} \\ Y^{M_i} \\ Z^{M_i} \end{bmatrix} = -q_{M_i}S\vec{T}_{BM_i}^{-1}\begin{bmatrix} C_X^{M_i} \\ C_Z^{M_i} \\ 0 \end{bmatrix}$$

$$\begin{bmatrix} L^{M_i} \\ M^{M_i} \\ N^{M_i} \end{bmatrix} = -q_{M_i}SD\vec{T}_{BM_i}^{-1}\begin{bmatrix} C_l^{M_i} \\ 0 \\ C_m^{M_i} \end{bmatrix} \tag{11}$$

Aerodynamic forces and moments are input to characterize the flight mechanics. The equations of motion are formulated in the inertial frame while the body frame was used for collection of aerodynamic data. The Earth coordinate system (subscript E) and the body-fixed coordinate system (subscript B) are related by the Euler angles for roll (ϕ), pitch (θ), and yaw (ψ) as shown in figure 3.
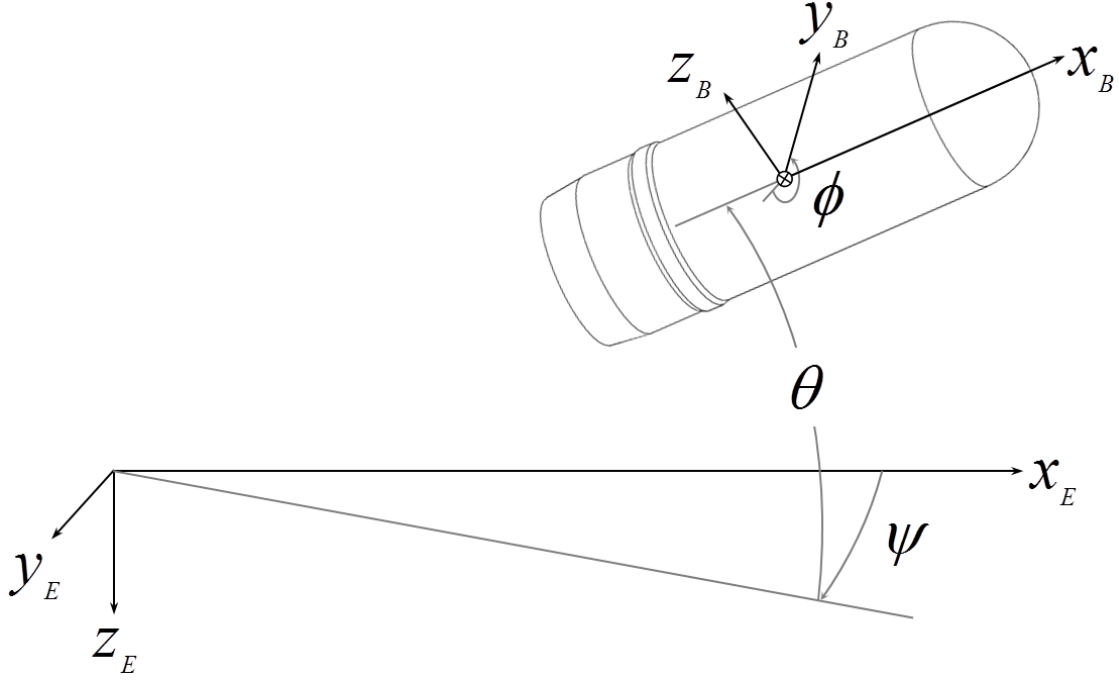
Figure 3. Earth and body-fixed coordinate systems and Euler angles.

The 6-degrees-of-freedom model was applied to analyze the flight mechanics (*22*). Equations for the translational and rotational kinematics in the body-fixed coordinate system are given.

$$\begin{bmatrix} \dot{x} \\ \dot{y} \\ \dot{z} \end{bmatrix} = \begin{bmatrix} c_\theta c_\psi & s_\phi s_\theta c_\psi - c_\phi s_\psi & c_\phi s_\theta c_\psi + s_\phi s_\psi \\ c_\theta s_\psi & s_\phi s_\theta s_\psi + c_\phi c_\psi & c_\phi s_\theta c_\psi + s_\phi s_\psi \\ -s_\theta & s_\phi c_\theta & c_\phi c_\theta \end{bmatrix} \begin{bmatrix} u \\ v \\ w \end{bmatrix} \tag{12}$$

$$\begin{bmatrix} \dot{\phi} \\ \dot{\theta} \\ \dot{\psi} \end{bmatrix} = \begin{bmatrix} 1 & s_\phi t_\theta & c_\phi t_\theta \\ 0 & c_\phi & -s_\phi \\ 0 & s_\phi/c_\theta & c_\phi/c_\theta \end{bmatrix} \begin{bmatrix} p \\ q \\ r \end{bmatrix} \tag{13}$$

Applying Newtonian kinetics to a projectile in free-flight results in the following translational and rotational dynamics expressions.

$$\begin{bmatrix} \dot{u} \\ \dot{v} \\ \dot{w} \end{bmatrix} = \frac{1}{m} \begin{bmatrix} X + X_G \\ Y + Y_G \\ Z + Z_G \end{bmatrix} - \begin{bmatrix} 0 & -r & q \\ r & 0 & -p \\ -q & p & 0 \end{bmatrix} \begin{bmatrix} u \\ v \\ w \end{bmatrix} \tag{14}$$

$$\begin{bmatrix} \dot{p} \\ \dot{q} \\ \dot{r} \end{bmatrix} = \vec{I}^{-1} \begin{bmatrix} L \\ M \\ N \end{bmatrix} - \vec{I}^{-1} \begin{bmatrix} 0 & -r & q \\ r & 0 & -p \\ -q & p & 0 \end{bmatrix} \vec{I} \begin{bmatrix} p \\ q \\ r \end{bmatrix} \tag{15}$$

The aerodynamics are computed as shown in equations 14 and 15, and the gravity force is found by

$$[X_G \quad Y_G \quad Z_G]^T = \vec{T}_{BE}^T [0 \quad 0 \quad g]^T \tag{16}$$

The flight control command for this concept is the desired maneuver direction (ϕ_{CMD}). To isolate the controlled flight performance we assume that the actuator responds sufficiently faster than the airframe ($\phi_{CMD} = \phi_C$) so that actuator dynamics may be neglected. Complementary studies have been performed (*13*) to ensure that desired and realized commands closely match.

A simple feedback concept is proposed to minimize cost. A strap-down detector provides the location of the target in the image plane. Details concerning whether these data arrive from a laser-designated spot detector or through image-based navigation are irrelevant for this study. Models representing target detection based on the flight mechanics are derived. The relative position of the target assuming that the detector is aligned with the projectile body coordinates is formulated.

$$\vec{r}_{PT}^B = \vec{T}_{BE}^T (\vec{r}_{OT}^I - \vec{r}_{OP}^I) \tag{17}$$

The roll angle present in the transformation matrix yields a rapidly changing target location as seen by a strap-down detector for a spin-stabilized projectile.

In practice, a passive detector obtains only the lateral relative positions and the actual distance is scaled based on the lens properties.

$$\begin{bmatrix} \epsilon_y \\ \epsilon_z \end{bmatrix} = \frac{f_L}{f_L - r_{PT}^B(1)} \begin{bmatrix} r_{PT}^B(2) \\ r_{PT}^B(3) \end{bmatrix} \tag{18}$$

Roll estimation is necessary to resolve the target error components in the fixed-plane (i.e., nonspinning) coordinate system. Devices such as magnetometers have been demonstrated to provide roll (*23–26*).

$$\begin{bmatrix} \tilde{\epsilon}_y \\ \tilde{\epsilon}_z \end{bmatrix} = \begin{bmatrix} \cos\phi & -\sin\phi \\ \sin\phi & \cos\phi \end{bmatrix} \begin{bmatrix} \epsilon_y \\ \epsilon_z \end{bmatrix} \tag{19}$$

These nonlinear flight models were implemented in simulation. Input data for the mass properties were obtained from solid modeling and from semi-empirical aeroprediction, wind tunnel, and computational fluids dynamics analyses for the aerodynamics (*11*). Some sample flight simulation output is provided to illustrate key aspects of the system.

Gun rifling imparts high spin to projectiles to ensure gyroscopic stability. Spin stabilization leads to incredibly accurate ballistic systems but complicates the flight behaviors. The spinning body motion produces Magnus moments (*27*) that often result in bounded dynamic instabilities that manifest in the flight as a coning motion. The system under investigation was launched with conditions necessary to fly to a ballistic range of 200 m. The angular motion over the entire flight (with no initial angular body rates) is shown in figure 4. The amplitude of the coning varies over the flight but is usually around 1°. The direction of the coning is counter-clockwise when viewed from behind the projectile. Aeromechanics theory (*22*) dictates that this coning occurs at a natural frequency of about 2 Hz for this projectile. The Magnus moment is often highly nonlinear

with angle of attack (e.g., maneuvering flight alters the response) and can feature considerable round-to-round variation due to manufacturing tolerances, atmospheric conditions, etc., so the data in figure 4 only illustrates the concept.
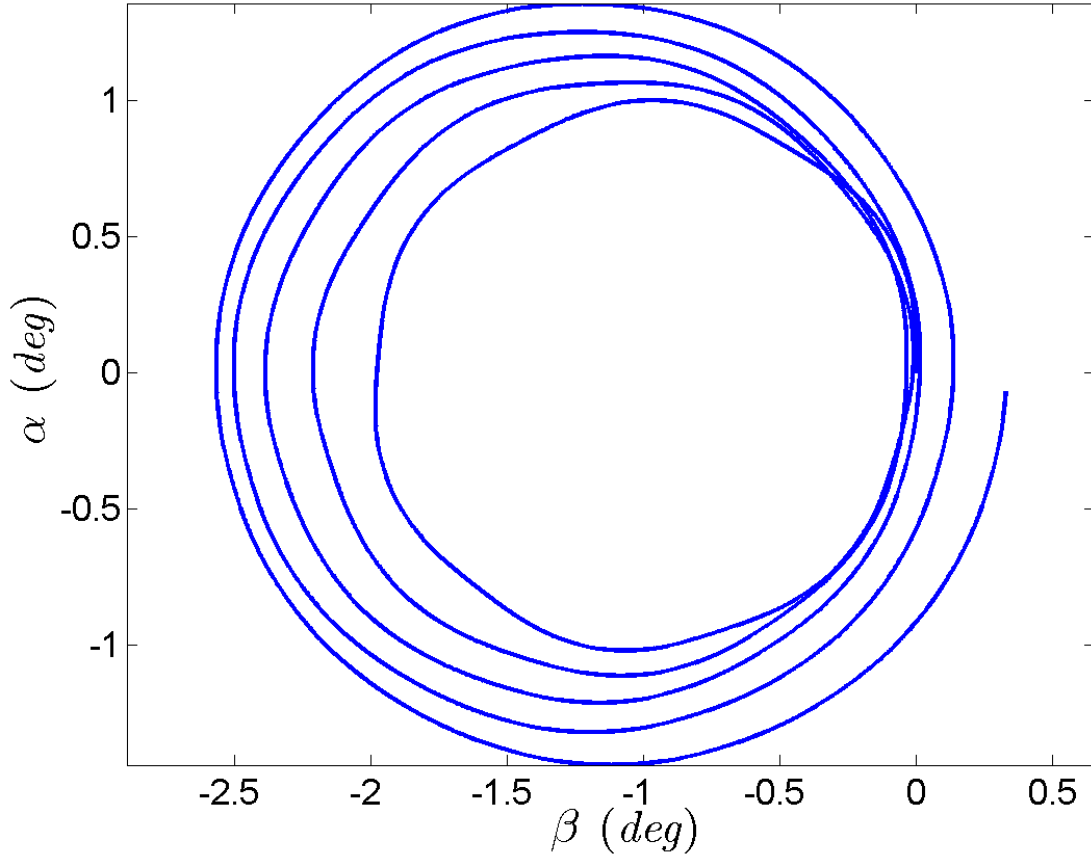

Figure 4. Angular motion for ballistic flight.

Another important result shown in figure 4 is the bias in the yaw angle of attack to about −1°. This phenomenon, known as yaw of repose (*22*), is due to the spinning body in atmospheric flight in the presence of gravity and yields a cross-range drift. This drift is evident in figure 5 as the trajectory bends over 1 m in the cross-range direction over 200 m of downrange travel. The center-of-gravity motion of the projectile also weaves back and forth, or swerves, as a result of the coning action.
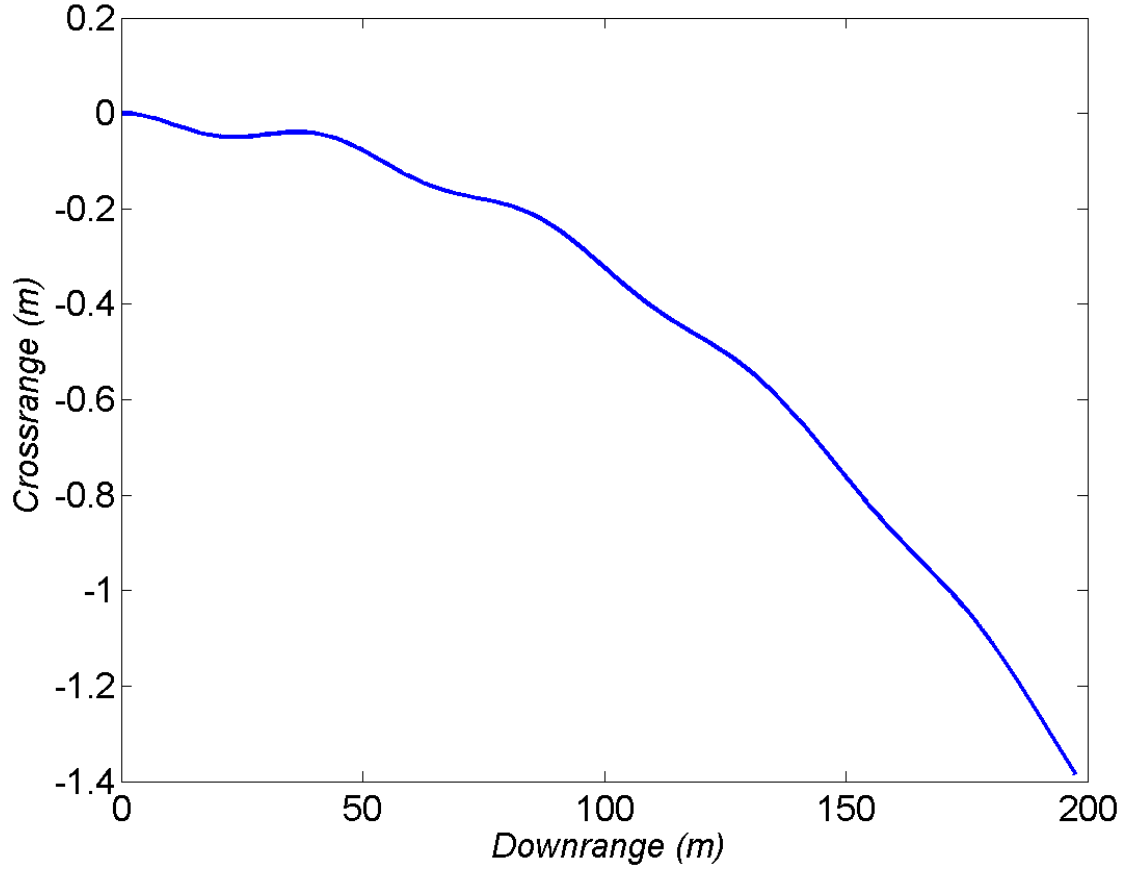
Figure 5. Swerve motion for ballistic flight.

Past work (*16, 17*) has proved that flight instabilities occur for spin-stabilized projectiles maneuvering perpendicular to the gravity field when the control effectiveness is sufficiently high. The potential for this instability exists in the current application. Figure 6 demonstrates large amplitude angular motion (counterclockwise direction when viewed from behind projectile) typical of flight instability. These results were obtained by increasing the aerodynamic force and moment of the wing by a factor of three in the nonlinear simulations. The implications of this instability mechanism are that while it is difficult to maneuver small-diameter spin-stabilized projectiles, there is an upper limit on the control authority that is not very high.
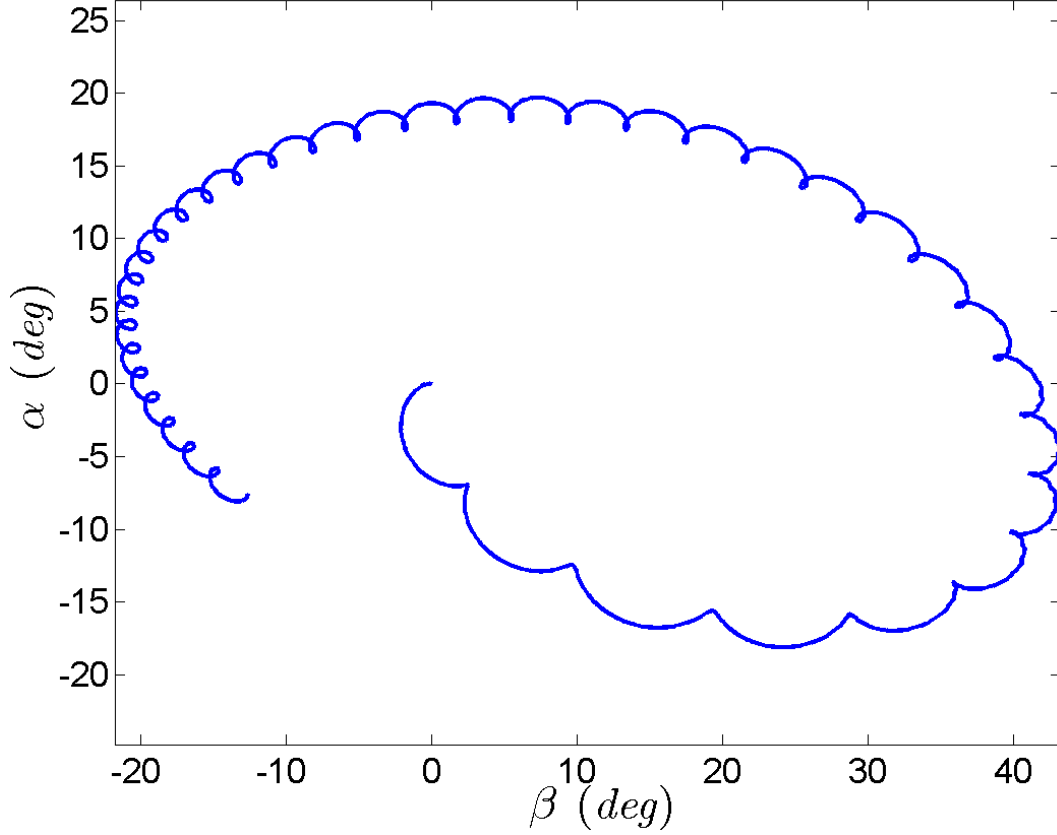
Figure 6. Instability of spin-stabilized projectile with high control effectiveness.

4. Guidance and Flight Control

Line-of-sight rate and closing velocity estimates are used to form proportional navigation commands in classical guidance schemes. Accelerometers and gyroscopes often supply additional necessary feedback. The accelerometers ensure that the airframe is maneuvering the center of gravity to intercept the target and the gyroscopes help damp unwanted angular motion. This scheme may not be applied to the current situation for a variety of reasons.

Low-cost measurement devices are severely stressed in the spin-stabilized environment. For example, accelerometers suffer from errors in bias, scale factor, misalignment, and misposition. Figure 7 shows a true and measured component of lateral acceleration for a typical maneuvering flight of the concept under investigation in this study. In practice, the device cannot be placed exactly on the spin axis due to manufacturing tolerances (especially at low cost). As a result, high acceleration from the fast-spinning axis bleeds over into the lateral channels and may overwhelm the true lateral acceleration. There is also significant high-frequency content in the signal at the spin rate (approximately 60 Hz) as shown in the oscillations for the zoomed-in portion of the measured acceleration.
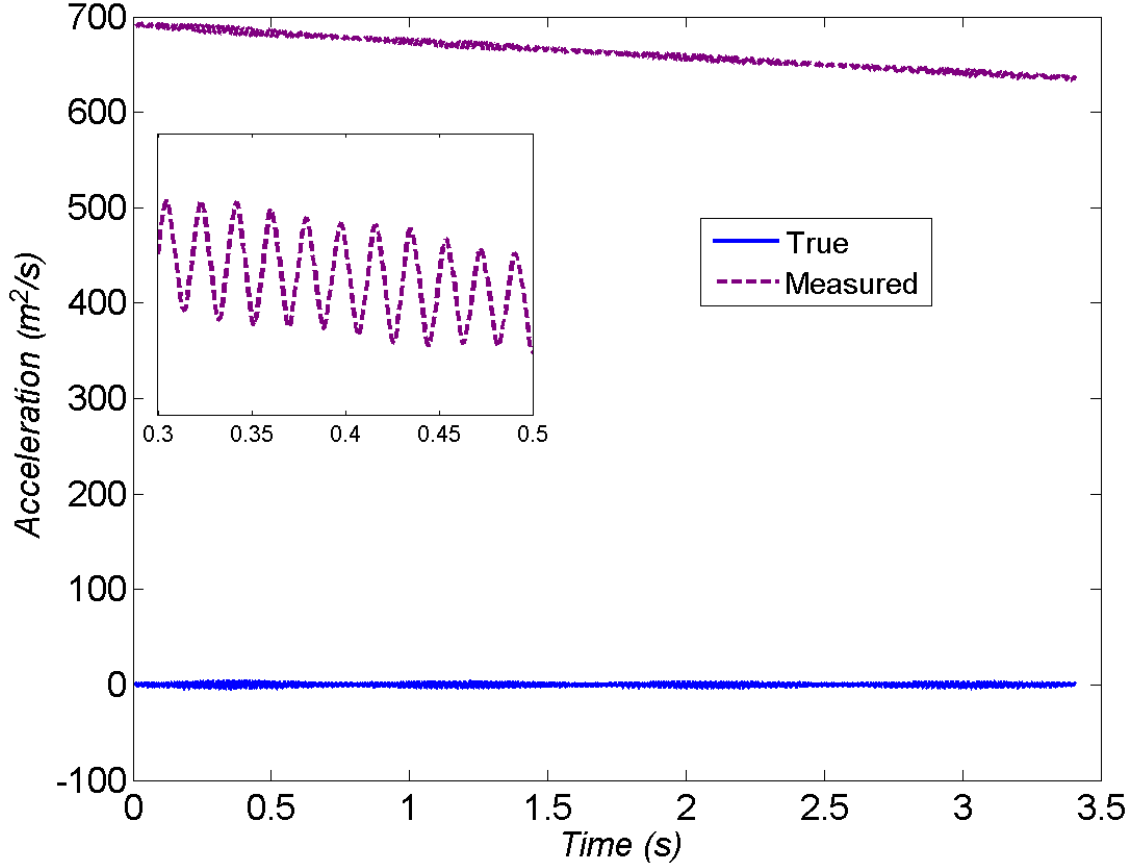
Figure 7. True and measured lateral accelerometer signal for ballistic flight.

Similar arguments apply to gyroscope measurements in this environment. Furthermore, even if quality gyroscope measurements were available, the aerodynamic control concept does not lend itself to damping the body angular rate.

This study proposes to use a detector as the minimal feedback measurement. In the strap-down detector plane, the target rotates at the spin rate and superposes the motion due to the trajectory arc and the coning. This action, along with a time of flight on the order of seconds, precludes high-accuracy estimation of line-of-sight rate from a low-cost detector. For these reasons, this study simply uses the raw detector plane data transformed by the roll angle as given in equations 18 and 19 for feedback purposes.

The basic structure shown in figure 8 can be applied to summarize the reduced-state control techniques proposed in this report. The loop in figure 8 is used in the cross-range and downrange directions. The nonlinear system dynamics formulated in the flight models above is contained in the function $\vec{H}$. The measurements are the detector data, $\vec{y} = [\tilde{\epsilon}_y \quad \tilde{\epsilon}_z]^T$. The error signal is formed by subtracting a reference from the feedback. The reference in the cross-range direction is zero but the downrange direction is nonzero to account for the trajectory arc. The control

consists of the magnitude and direction of maneuver. This integrated guidance and control approach resembles that found in the literature for missiles (*28–30*) in that enhanced performance is sought through minimal feedback.

$$\vec{u} = \left[K_\epsilon \sqrt{\tilde{\epsilon}_y{}^2 + (\tilde{\epsilon}_z - \tilde{r}_z)^2} \quad \tan^{-1} \frac{-(\tilde{\epsilon}_z - \tilde{r}_z)}{-\tilde{\epsilon}_y} \right]^T \qquad (20)$$
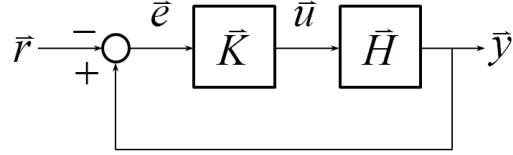
Figure 8. Basic control structure.

If a zero reference were used in the downrange direction, the projectile would unnecessarily spend valuable control effort trying to maneuver toward the ground due to the trajectory arc. A reference signal representing the curvature of the trajectory that can be estimated preflight overcomes the problems of a zero reference. Technologies such as a weapon fire control system or attitude estimation onboard the projectile using magnetometers can supply an approximate launch angle. The muzzle velocity, mass properties, and aerodynamics are relatively fixed entities that enable a downrange reference to be formed specific to that particular launch angle. An example of a reference signal for a launch angle of about 15° is presented in figure 9. These data may be used as a function of time of flight to effectively zero the target location on the detector in the downrange direction.
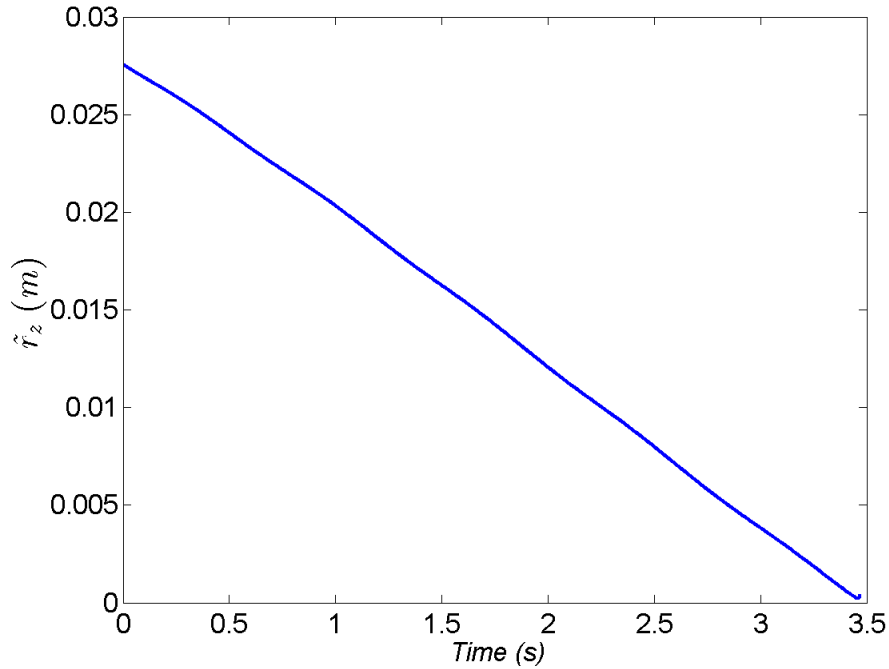
Figure 9. Representative downrange reference signal.

The nonlinear dynamics for this problem along with the limitations of practical measurements prohibits the classic control design method based on finding a linear relationship between the control input and feedback output. Rather, data obtained from nonlinear simulations were used to obtain a relationship between the control magnitude and detector response. In this approach, it is critical that the theory and data in the simulations are appropriate, which is supported in complementary literature (*10–13*).

Nonlinear simulations were conducted wherein open-loop maneuvers were commanded at different magnitudes and directions (i.e., to cause the projectile to travel left, right, up, or down). The resulting response data due to these maneuvers was collected. More specifically, the relative position (equation 21) and velocity (equation 22) of the projectile with respect to the target in velocity vector coordinates were tabulated.

$$\vec{r}_{PT}^{V} = \vec{T}_{VE}^{T}(\vec{r}_{OT}^{I} - \vec{r}_{OP}^{I}) \tag{21}$$

$$\vec{r}_{P/T}^{V} = \vec{r}_{P/T}^{I} - \frac{\vec{r}_{OP}^{I} \times \vec{r}_{P/O}^{I}}{|\vec{r}_{OP}^{I}|^2} \times \vec{r}_{PT}^{V} \tag{22}$$

System identification and parameter estimation was used on this nonlinear simulation data to build and populate a model to use linear systems theory in determining the gains. To isolate the control dynamics, the ballistic response was subtracted from the data collected during the maneuvering flights. A second-order model with a forcing function was offered to capture the essential elements of the system dynamics based on inspection of these data.

$$\ddot{\varepsilon} + 2\xi\omega_n\dot{\varepsilon} + \omega_n^2\varepsilon = f_\mu\mu \tag{23}$$

This model was implemented in a parameter estimation algorithm to obtain data necessary for selecting gains based on linear systems theory. A maximum likelihood method was applied to find the model parameters (*31, 32*). This nonlinear technique uses measurements to seek model parameters that minimize a cost function. The states for this problem were the detector error rates and errors, $\vec{x} = [\dot{\varepsilon} \quad \varepsilon]^{\mathrm{T}}$. Measurements of these states were supplied by the nonlinear simulation as described and predictions of these states were based on propagating the model in equation 23 forward in time. The control was the input multiplied by a scaling. The value of μ was the fraction of the baseline control effectiveness used in the nonlinear flight simulation ($0 < \mu < 1$). The parameter vector was formulated given these models.

$$\vec{\theta} = [\xi \quad \omega_n \quad f_\mu]^{\mathrm{T}} \tag{24}$$

An example of this analysis is shown in figure 10. Four levels of baseline control effectiveness (0.25, 0.50, 0.75, and 1.00) were investigated with a maneuver to extend range. The circles represent the measurements from the nonlinear flight simulation and the curves are from the parameter estimation with the surrogate model. Oscillations in the nonlinear response due to angular motion increase with control effectiveness. The simplified model cannot reproduce specific aspects of the highly nonlinear dynamics; however, the essential features regarding how

the control influences the detector response are captured. In any event, this surrogate model is used to aid gain selection prior to control performance assessment in nonlinear flight simulations. Model parameters from the estimation are provided in table 1.
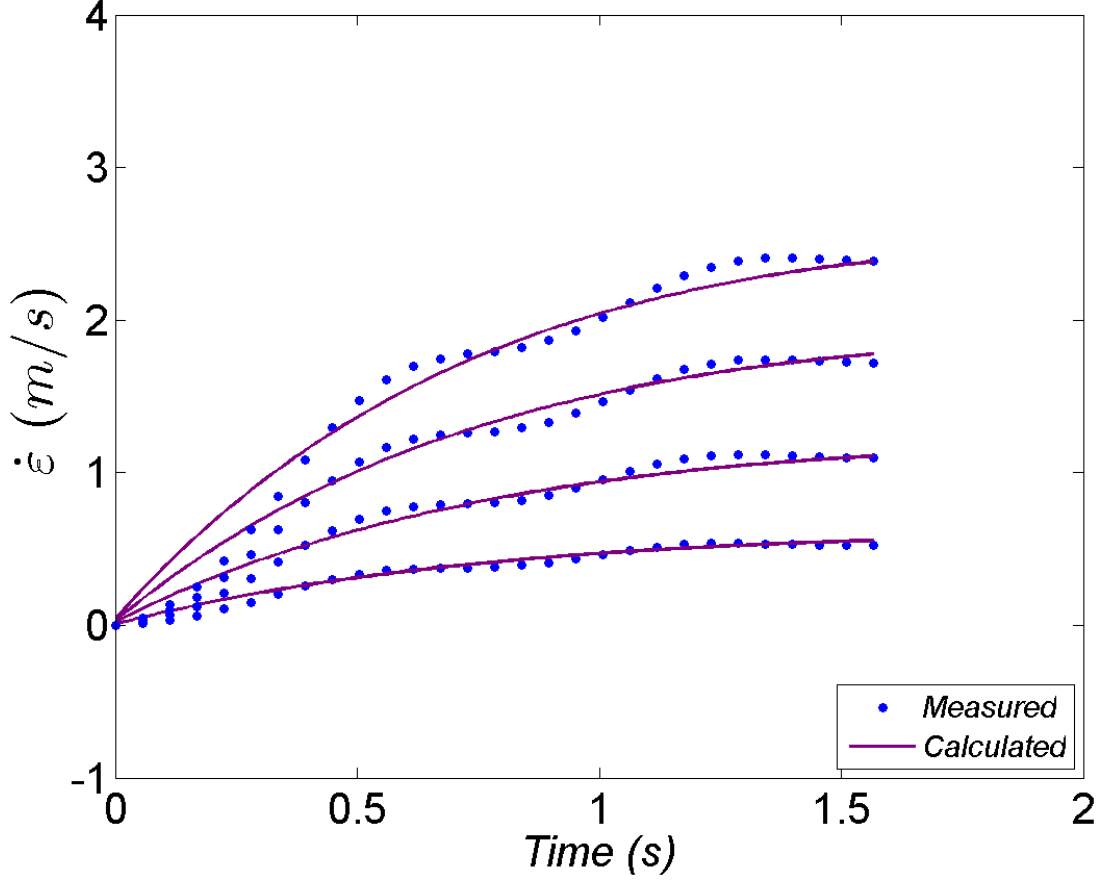

Figure 10. Parameter estimation for different control magnitudes.

Table 1. Parameter estimation data.

ξ ()	ω_n (rad/s)	f_μ (m/s^2)
2.5106	0.26061	3.6356

Model formulation and parameter estimation results enable control design. The control system dynamics can be expressed mathematically with the previously stated definitions of the state vector and control. An error rate gain does not appear in equation 25 because the overarching reduced-state feedback approach proposed in this study (and shown in equation 20) is to use simple position errors in the detector plane. The relationship between the gain in the surrogate model and the control law used in the nonlinear flight simulation is trivial ($K_\epsilon = K_\varepsilon f_\mu$).

$$\vec{A}_C = \begin{bmatrix} -2\xi\omega_n & -\omega_n^2 - K_\varepsilon \\ 1 & 0 \end{bmatrix} \tag{25}$$

Equipped with the parameter estimates and equation 25, investigation of the system structure was undertaken. Figure 11 shows the eigenvalues as a function of the gain. These data indicate the system is always stable. As the gain increases, the system undergoes a change from critically damped to oscillatory behavior. The manner in which the damping ratio decreases as the gain increases is critically important for this application since damping is not explicitly used in the feedback. This analysis was used to select initial values for the control gain used in the nonlinear flight simulation.
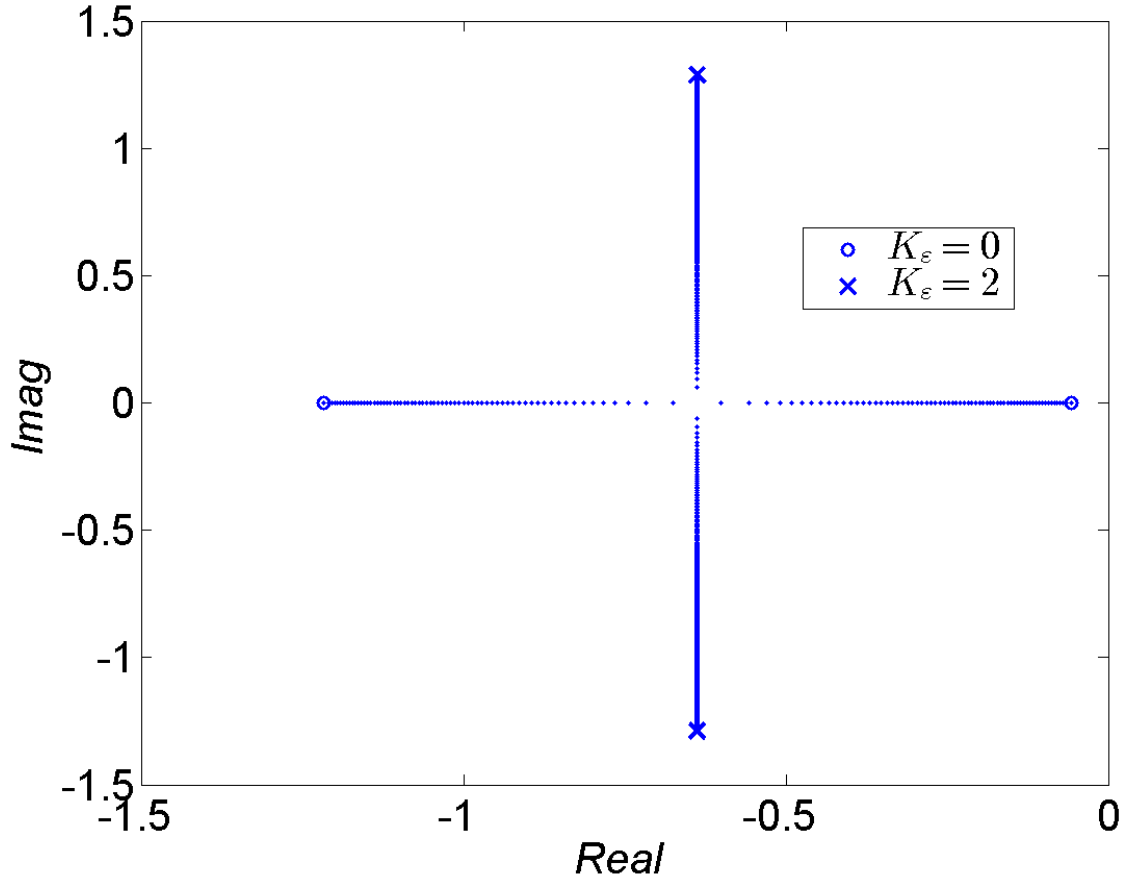

Figure 11. Eigenvalues for different values of gain.

The goal now is to relate gains from the surrogate model used for parameter estimation and linear analysis (e.g., equation 26) to gains in the nonlinear controller with the strap-down detector (equations 18–20) through model equivalency. An expression for the rate of change of the detector error in the body frame is given.

$$\dot{\vec{\epsilon}}^B = \frac{f_L}{\left(\dot{r}_{P/T}^B(1) - f_L\right)^2} \vec{r}_{PT}^B + \frac{f_L}{f_L - r_{PT}^B(1)} \left(\dot{\vec{r}}_{P/T}^I - \vec{\omega}_{B/I} \times \vec{r}_{PT}^B\right) \tag{26}$$

The lens properties may be added to the equations for the position and velocity in the velocity vector coordinates to model a detector mounted in the velocity vector coordinates. The velocity vector-mounted and strap-down (body-mounted) detector models are summarized in table 2. Comparing these detector models in table 2 highlights some structural similarities.

Table 2. Detector models for position and velocity of target.

Coordinates	Position	Velocity
Velocity vector	$\vec{\epsilon}^V \dfrac{f_L}{f_L - r_{PT}^V(1)} \vec{r}_{PT}^V$	$\vec{\epsilon}^V = \dfrac{f_L}{\left(\dfrac{\dot{r}_P^V(1)}{T} - f_L\right)^2} \vec{r}_{PT}^V$ $+ \dfrac{f_L}{f_L - r_{PT}^V(1)}\left(\vec{r}_{P/T}^I - \vec{\omega}_{V/I} \times \vec{r}_{PT}^V\right)$
Body fixed	$\vec{\epsilon}^B \dfrac{f_L}{f_L - r_{PT}^B(1)} \vec{r}_{PT}^B$	$\vec{\epsilon}^B = \dfrac{f_L}{\left(\dfrac{\dot{r}_P^B(1)}{T} - f_L\right)^2} \vec{r}_{PT}^B$ $+ \dfrac{f_L}{f_L - r_{PT}^B(1)}\left(\vec{r}_{P/T}^I - \vec{\omega}_{B/I} \times \vec{r}_{PT}^B\right)$

For model equivalency purposes, assume that the airframe flies at low total angle of attack so that $\vec{\epsilon}^B \approx \vec{\epsilon}^V$. This assumption will be further supported with an observer designed to remove excess angular motion.

We define states $\vec{x}_e = [\dot{e} \quad e]^T$ and controls $\vec{u}_e = -K_e \vec{x}_e$ with a component of the detector error e. Assume $\dot{r}_{P/T}^V(1) = \bar{V}$ and $r_{PT}^V(1) = \bar{V}t$ since the forward velocity dominates the velocity vector and velocity decay is small over these flights. The following relationships are defined between the velocity vector-mounted (i.e., surrogate) model in equation 23 and the strap-down detector model.

$$\dot{e} = \frac{f_L}{(\bar{V} - f_L)^2}\varepsilon + \frac{f_L}{f_L - \bar{V}t}\dot{\varepsilon} \tag{27}$$

$$e = \frac{f_L}{f_L - \bar{V}t}\varepsilon \tag{28}$$

Similar to equation 23, the expressions in equations 27 and 28 apply to both lateral components [e.g., $\epsilon^V(2)$, $\epsilon^V(3)$]. Next, equate the controls of the two models by setting $\mu = u_e$ and manipulating along with equations 27 and 28 to yield the final relationship for gains.

$$K_e = \frac{f_L - \bar{V}t}{f_L}\frac{K_\varepsilon}{f_\mu} = K_\epsilon \tag{29}$$

This expression provides a means to analyze the control system using surrogate modeling and then apply the appropriate scaling to the full nonlinear controller. The nonlinear control gain features a linear term with time of flight. The lens properties, flight velocity, and surrogate model control scaling also influence the gain.

An observer was constructed to remove excess angular motion in the strap-down detector attributable to nonlinear spin-stabilized flight dynamics (e.g., fast and slow modes or angular motion, yaw of repose). The measurement model follows.

$$\begin{bmatrix} \tilde{\epsilon}_y^* \\ \tilde{\epsilon}_z^* \end{bmatrix} = \begin{bmatrix} \tilde{r}_y^* + \tilde{r}_S^* sin(\omega_S t + \gamma_S) + \tilde{r}_F^* sin(\omega_F t + \gamma_F) \\ \tilde{r}_z^* + \tilde{r}_S^* cos(\omega_S t + \gamma_S) + \tilde{r}_F^* cos(\omega_F t + \gamma_F) \end{bmatrix} \tag{30}$$

The basic premise of this estimator is that flight dynamic theory (*22*) may be applied to determine epicyclic motion (i.e., fast and slow modes) in the detector and the remaining signal is attributable to the error in heading to the target. The fast and slow mode frequencies and phase shifting for right-hand gun rifling can be predicted a priori. This leaves the following states for this problem.

$$\vec{x}^* = [\tilde{r}_S^* \quad \gamma_S \quad \tilde{r}_F^* \quad \gamma_F \quad \tilde{r}_y^* \quad \tilde{r}_z^*]^T \tag{31}$$

This model and states were implemented in a Kalman filter assuming that each variable in the state vector is constant between measurement updates. The measurement input was the nonlinear detector model in fixed-plane coordinates (equation 19) with the downrange reference ($\tilde{r}_z$) applied. The output of this estimator was used in the flight controller (equation 20).

5. Results

These guidance and control techniques were implemented in the nonlinear flight simulations to assess performance. In practice, ballistic delivery of a lethal payload has errors due to effects such as muzzle velocity variation, imperfect targeting and aiming, manufacturing tolerances, fuzing, and atmospheric disturbances. When adding guidance components, errors due to corrupted measurements and actuator performance must be considered. Models and input data to account for these error sources were incorporated along with Monte Carlo techniques into the flight analysis (*11*, *33*)

Simulations were conducted using this reduced-state guidance approach. Shown in figure 12 is a representative fixed-plane output of the target motion in the detector plane (applying the reference in the downrange direction) from a guided flight with uncertainties to a target at 200 m. The blue curves represent the cross-range data and the purple curves are for the downrange direction. The raw and estimated body fixed signals are given along with the velocity vector signal. The downrange reference signal has been applied to all curves. High- and low-frequency content is evident in the raw body fixed data. The projectile epicyclic motion adds

complexity to the detector signal, which may lead to poor guidance performance. Fortunately, the dynamics of the epicycle are included in the estimator. The filtered data effectively removes the fast and slow mode motion so that only the heading error remains. The detector error in velocity vector coordinates (top-left equation in table 2) is provided in figure 12 as a baseline for comparing the filtered body fixed data. While impractical, the detector signal in velocity vector coordinates may provide optimal feedback for this problem. There is consistency between the filtered body fixed and velocity vector signals but agreement is not perfect.
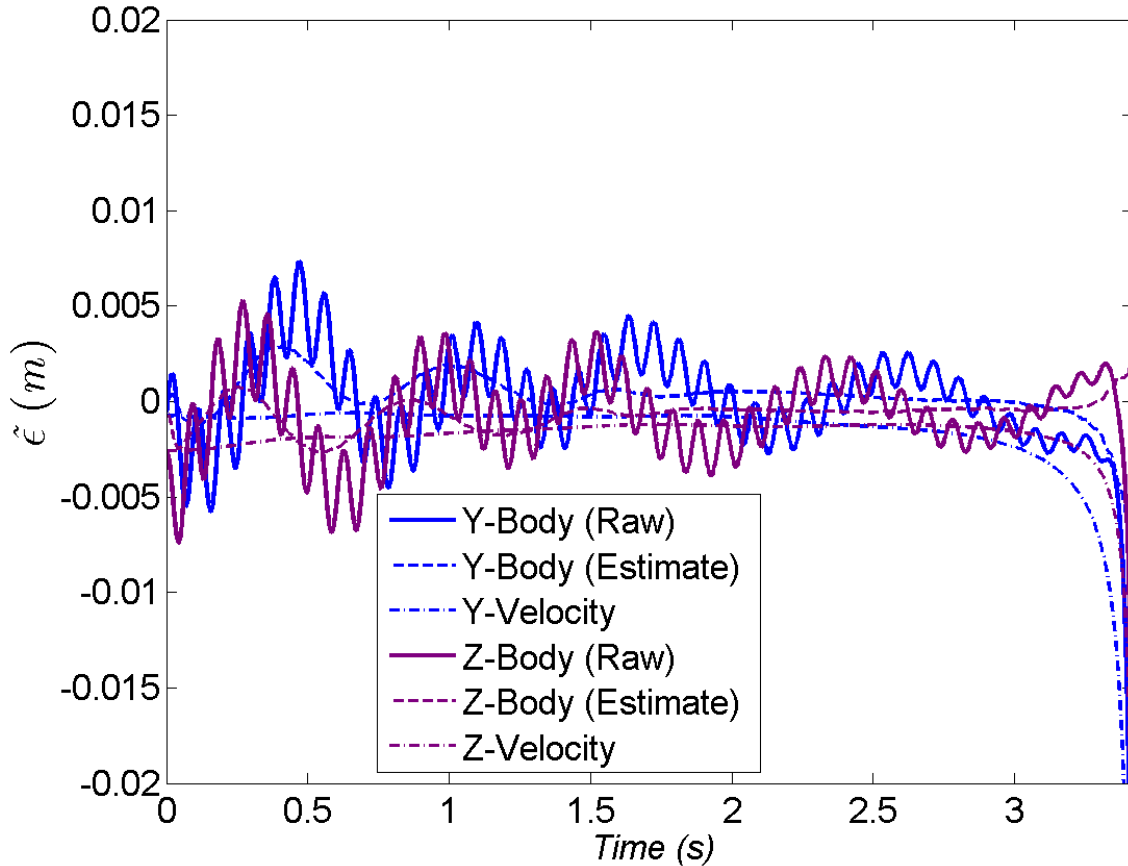

Figure 12. Representative error signals for guided flight.

According to the filtered feedback signals in figure 12, the projectile flies with relatively low error in the cross-range direction. The downrange error grows to negative values, indicating that perhaps the weapon was aimed too low or the muzzle velocity was slower than expected. Regardless, control commands to maneuver the projectile away from the ground should result from this feedback signal. Poor control commands would result from using the raw body fixed signal since the magnitude of the fast and slow mode oscillations are the same or greater than the remaining heading error. The finite error magnitude in figure 12 at the end of the flight underscores the difficulty in sufficiently maneuvering small-diameter spin-stabilized projectiles without inducing instability.

18

Control commands resulting from using raw body fixed signals in figure 12 for feedback is given in figure 13a. The blue circles representing the maneuver direction have the scale on the left-hand axis. The green diamonds represent the maneuver magnitude with the scale on the right side of the plot. Cascading of the angular and swerving motion of the projectile through the feedback and into the control commands is evident in the data of figure 13a. The commanded maneuver direction oscillates in all directions since the magnitude of the signal attributable to the fast and slow mode motion is equal to or greater than the actual heading error. The control amplitude also quickly saturates yielding high angle-of-attack flight dynamic instabilities as described for figure 6. The nonlinear dynamics inherent to this class of flight bodies yields feedback responses on the same order as the control action.

The subsequent control commands based on the filtered error signals shown in figure 12 is provided in figure 13b. The utility of feedback that includes the flight dynamics in the estimation algorithm is rapidly apparent when contrasting figures 13a and 13b. The control commands in figure 13b are much smoother. Consistent with the discussion for the filtered error signal, the algorithm generally commands the projectile to maneuver up to compensate for the launch or flight errors (e.g., low aim angle, low muzzle velocity). The magnitude of the maneuver remains around 0.25 over the flight eventually reaching saturation shortly before impact.
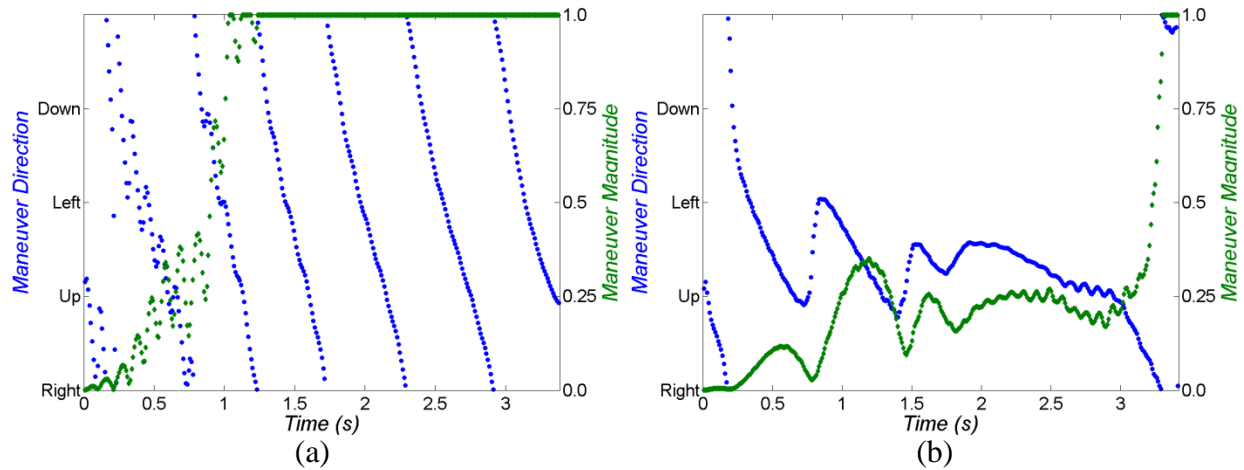

Figure 13. Representative control commands for guided flight: control commands resulting from using raw body fixed signals in figure 12 (a) and control commands based on the filtered error signals in figure 12 (b).

The modeling, parameter estimation, and stability analysis for control design was critical to successful guidance in the nonlinear simulations. The control gain used in nonlinear simulations was one that is consistent with the values obtained in the linear analysis (figure 11). The adaptive gain scheme (i.e., linearly increasing with time) proposed in equation 29 provided sufficient control commands while still keeping the angle of attack sufficiently small. Dynamic flight instabilities such as that illustrated in figure 6 were encountered when higher gains were used early in flight for simulations conducted without the adaptive gain scheme.

The angular motion produced by the control commands of figure 13b based on the filtered feedback in figure 12 is presented in figure 14. Launch disturbances yield angular motion amplitude around 2° in both the fast and slow mode. The epicycle damps throughout flight, but the Magnus moment for this flight vehicle excites the slow mode. The "up" guidance commands through a majority of this flight result in a slightly positive pitch angle of attack. The yaw angle of attack has a small negative value mainly due to yaw of repose. Both pitch and yaw angles of attack increase near impact since the maneuver magnitude saturates.
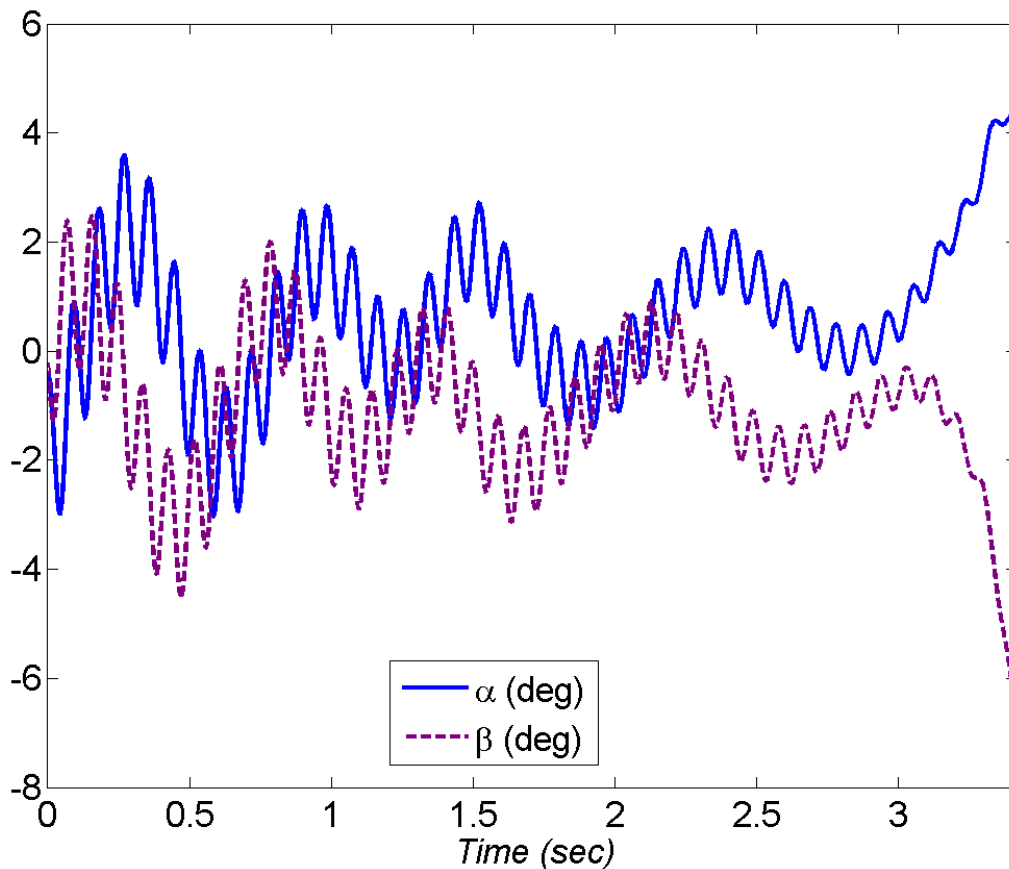

Figure 14. Angular motion history.

The trajectory is shown in figure 15. The center of gravity reaches almost 14 m in altitude to fly about 200 m downrange in just under 3.5 s. This representative guided flight impacted about 1 m from target in contrast to the same flight without any guidance, which landed about 10 m away.
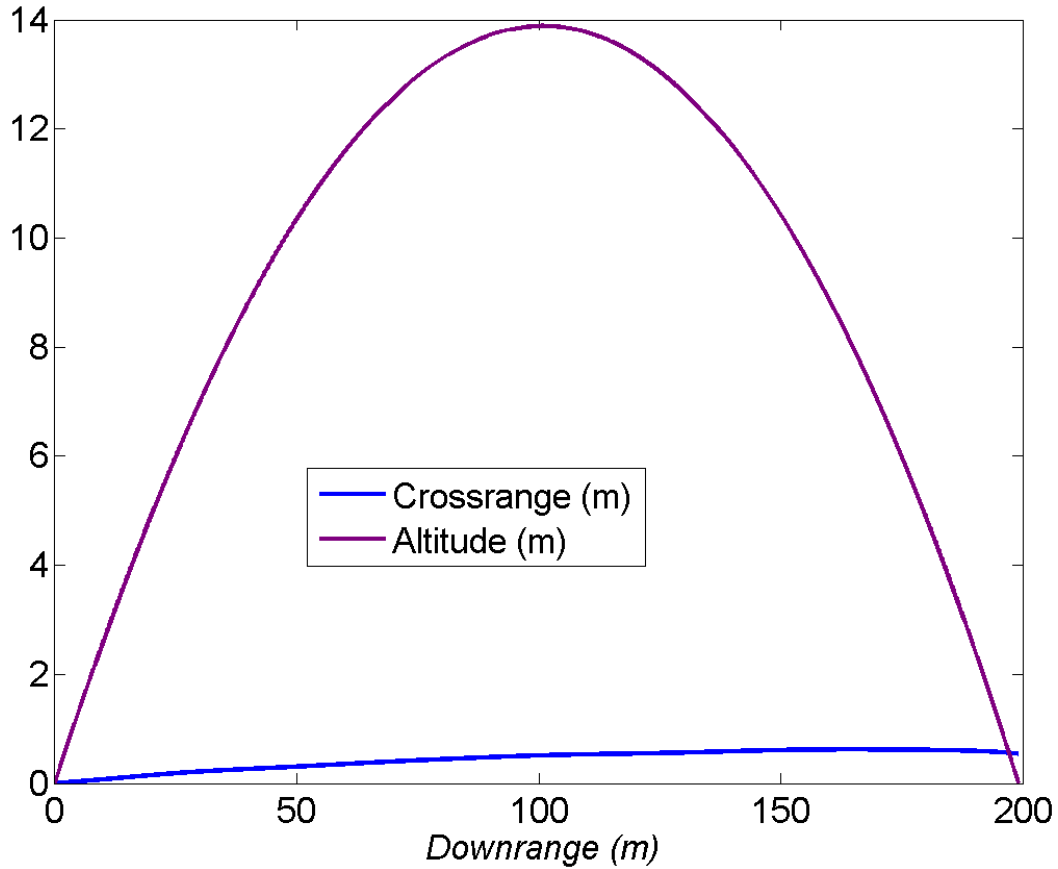
Figure 15. Trajectory.

The delivery accuracy increase of the guided flight over the ballistic flight, especially since this is a proof of concept and the system is not optimized, is sufficient to enhance target effect and merits further consideration. Monte Carlo analysis was conducted on this system to determine fuller spectrum guided performance with respect to ballistic performance. The ballistic and guided impact locations resulting from a set of 100 Monte Carlo replications is provided in figure 16. Guided flights were conducted using three different feedback sources: raw body fixed, filtered body fixed, and velocity vector.
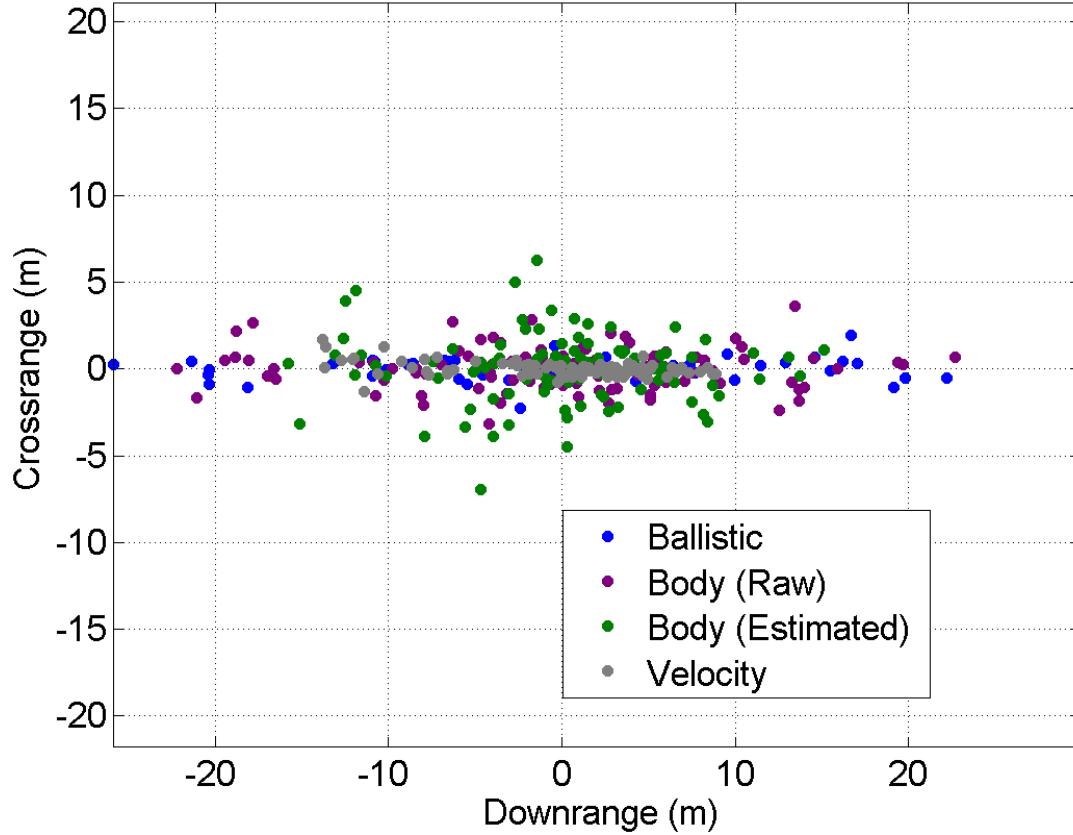
Figure 16. Impacts from Monte Carlo system simulations of ballistic and guided flight.

Ballistic impacts are spread along the downrange axis due to the launch angle (15°) and physics of the deliver error process (e.g., muzzle velocity variation). The guided flight tightens the impact grouping. As expected, the filtered body fixed feedback enhances performance over the raw body fixed feedback but does not perform as well as using the detector signal in velocity vector coordinates. Spread in the impact distribution does remain in the guided flights due to the difficulties discussed (e.g., coning and swerve motion, practical feedback limitations, and constraint on control authority due to instability) for small-diameter spin-stabilized projectiles.

The data shown in figure 16 feature many impact points lying on top of each other; therefore, these data are presented in a slightly different manner in figure 17. This histogram shows how this reduced-state guidance scheme reduces the miss distance from the ballistic system. The guided circular error probable is 3.1 m using detector feedback in velocity vector coordinates, 4.2 m with filtered body feedback, and 5.4 m with raw body feedback. The corresponding ballistic circular error probable is 8.6 m. These data support the hypothesis that guidance and control algorithms and novel concepts using low-cost measurement and maneuver components can be used to effectively guide small-diameter spin-stabilized projectiles. The main contributor to guidance error is the nonlinear dynamics (e.g., coning, swerve) of the projectile influencing the filtered detector feedback and the subsequent control input. Schemes to mitigate these issues, such as additional damping or improved state estimation, would improve performance.
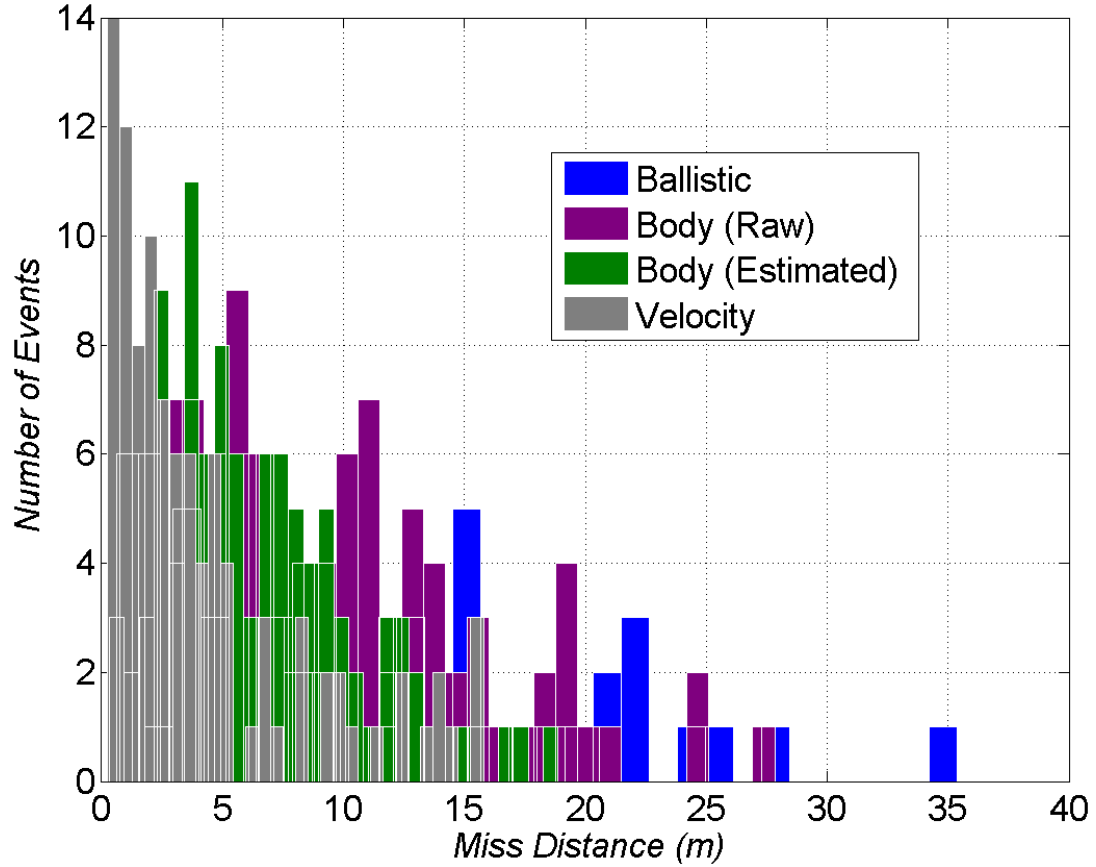
22

Figure 17. Histograms of impacts from Monte Carlo system simulations of ballistic and guided flight.

6. Conclusions

This report proposed a guidance and control approach incorporating small size and cost technologies applicable across a wide variety of infantry weapons. This effort is unique in the literature by considering not only the maneuverability (*12, 13*, *18–21*) and feedback measurements for small-diameter gyroscopically stabilized projectiles, but also the overall guided performance using a novel control scheme.

The concept was sketched and shown integrated into a 40-mm-diameter projectile package. A low-cost strap-down detector in the nose supplies feedback measurements. The lethal payload takes up the midbody and the maneuver mechanism is at the rear. The maneuver mechanism is innovative in using low-cost rotary motors to achieve high actuation frequencies necessary for spin-stabilized projectiles. A few different means of continuously varying the maneuver magnitude were discussed.

Nonlinear flight models of the aerodynamics, flight mechanics, actuators, and measurements were formulated and implemented in simulation to facilitate guidance and control design and test the hypothesis of this study. Key aspects of spin-stabilized projectile dynamics relevant to guidance, including short time of flight, coning, swerve, drift, and instability, were illustrated.

The classic guidance and control approach was summarized, and the inadequacy of this scheme for the current investigation was demonstrated through nonlinear simulation of corrupted accelerometer measurements. Unique reduced-state feedback control techniques were introduced. A reference signal was proposed for increasing guidance efficiency. The measurement and actuation components required to implement this control scheme are low cost and practical.

Modeling of the feedback-control response was undertaken to accommodate the extreme nonlinearities present in spin-stabilized dynamics. Parameter estimation routines were applied to obtain model parameters using nonlinear simulation data. Initial control design was performed using these models and parameters.

The guidance and control was investigated in nonlinear simulation that incorporated system uncertainties. The feedback and corresponding control commands from guided flights demonstrated the approach. Results highlighted the difficulties associated with guiding spin-stabilized projectiles such as using practical feedback in the presence of coning and swerve motion, and balancing control authority with instability.

Monte Carlo simulations were conducted to assess lethal payload delivery via ballistic and guided means. Delivery accuracy for a nonoptimized guided configuration was more than a factor of two better than the ballistic delivery suggesting that further research is warranted. Overall, this study supports the hypothesis that flight control algorithms and novel system concepts using low-cost sensor and actuator components can be used to effectively guide small-diameter gyroscopically stabilized projectiles.

7. References

1. Fresconi, F. E. Guidance and Control of a Projectile With Reduced Sensor and Actuator Requirements. *Journal of Guidance, Control, and Dynamics* **2011,** *34* (6), 1757–1766.

2. Ilg, M. *Framework for a Software-Defined Global Positioning System (GPS) Receiver for Precision Munitions Applications;* ARL-TR-5796; U.S. Army Research Laboratory: Aberdeen Proving Ground, MD, 2012.

3. Brown, T. G.; Davis, B.; Hepner, D.; Faust, J.; Myers, C.; Muller, P.; Harkins, T.; Hollis, M.; Miller, C.; Placzankis, B. Strap-Down Microelectromechanical (MEMS) Sensors for High-G Munition Applications. *IEEE Transactions on Magnetics* **2001,** *37* (1), 336–342.

4. Hubbard, K. *Characterization of Semi-Active Laser (SAL) Seekers for Affordable Precision Guidance of Gun-Launched Munitions;* ARL-TR-5233; U.S. Army Research Laboratory: Aberdeen Proving Ground, MD, 2010.

5. Fresconi, F. E.; Harkins, T. Experimental Flight Characterization of Asymmetric and Maneuvering Projectiles From Elevated Gun Firings. *Journal of Spacecraft and Rockets* **2012,** *49* (6), 1120–1130.

6. Graham, M. J.; Weinacht, P.; Brandeis, J. Numerical Investigation of Supersonic Jet Interaction for Finned Bodies. *Journal of Spacecraft and Rockets* **2002,** *39* (3), 376–383.

7. Morrison, P. H.; Amberntson, D. S. Guidance and Control of a Cannon-Launched Guided Projectile. *Journal of Spacecraft and Rockets* **1977,** *14* (6), 328–334.

8. Rogers, J.; Costello, M. Design of a Roll-Stabilized Mortar Projectile With Reciprocating Canards. *Journal of Guidance, Control, and Dynamics* **2010,** *33* (4), 1026–1034.

9. Burchett, B.; Costello, M. Model Predictive Lateral Pulse Jet Control of an Atmospheric Rocket. *Journal of Guidance, Control, and Dynamics* **2002,** *25* (5), 860–867.

10. Fresconi, F.; Cooper, G. R.; Celmins, I.; DeSpirito, J.; Costello, M. Flight Mechanics of a Novel Guided Spin-Stabilized Projectile Concept. *Journal of Aerospace Engineering* **2011,** *226,* 327–340.

11. Fresconi, F.; DeSpirito, J.; Celmins, I. *Flight Performance of a Man Portable Guided Projectile Concept;* ARL-TR-6840; U.S. Army Research Laboratory: Aberdeen Proving Ground, MD, 2012; accepted by *Journal of Spacecraft and Rockets,* 2014.

12. Gross, M.; Costello, M.; Fresconi, F. Impact Point Model Predictive Control of a Spin-Stabilized Projectile With Instability Protection. *Proceedings of the Atmospheric Flight Mechanics Conference,* Boston, MA, 19–21 August 2013.

13. Fresconi, F.; Celmins, I.; Nelson, B. *Actuator Characterization of Man Portable Precision Maneuver Concepts;* ARL-TR-6841; U.S. Army Research Laboratory: Aberdeen Proving Ground, MD, March 2014.

14. Ollerenshaw, D.; Costello, M. Simplified Projectile Swerve Solution for General Control Inputs. *Journal of Guidance, Control, and Dynamics* **2008,** *31,* 1259–1265.

15. Fresconi, F.; Plostins, P. Control Mechanism Strategies for Spin-Stabilized Projectiles. *Journal of Aerospace Engineering* **2010,** *224,* 979–991.

16. Lloyd, K. H.; Brown, D. P. Instability of Spinning Projectiles During Terminal Guidance. *Journal of Guidance, Control, and Dynamics* **1979,** *2* (1), 65–70.

17. Murphy, C. H. Instability of Controlled Projectiles in Ascending or Descending Flight. *Journal of Guidance, Control, and Dynamics* **1981,** *4* (1), 66–69.

18. McMichael, J.; Lovas, A.; Plostins, P.; Sahu, J.; Brown, G.; Glezer, A. Microadaptive Flow Control Applied to a Spinning Projectile. *Proceedings of the AIAA Flow Control Conference*, Portland, OR, 2004.

19. Abramson, P.; Vukasinovic, B.; Glezer, A. Direct Measurements of Controlled Aerodynamic Forces on a Wire-Suspended Axisymmetric Body. *Experiments in Fluids* **2011,** *50,* 1711–1725.

20. Abramson, P.; Vukasinovic, B.; Glezer, A. Fluidic Control of Aerodynamic Forces on a Bluff Body of Revolution. *AIAA Journal* **2012,** *50,* 832–843.

21. Cooper, G.; Costello, M. Flight Dynamic Response of Spinning Projectiles to Lateral Impulsive Loads. *Journal of Dynamic Systems, Measurement, and Control* **2004,** *126,* 605–613.

22. Murphy, C. H. *Free Flight Motion of Symmetric Missiles;* BRL-TR-1216; U.S. Army Ballistics Research Laboratory: Aberdeen Proving Ground, MD, 1963.

23. Rogers, J.; Costello, M. A Low-Cost Orientation Estimator for Smart Projectiles Using Magnetometers and Thermopiles. *Navigation* **2012,** *59* (1), 9–24.

24. Rogers, J.; Costello, M.; Harkins, T.; Hamaoui, M. Effective Use of Magnetometer Feedback for Smart Projectile Applications. *Navigation* **2011,** *58* (3), 203–219.

25. J. Maley. Roll Orientation from Commercial Off-The-Shelf (COTS) Sensors in the Presence of Inductive Actuators. *Proceedings of the Institute of Navigation Joint Navigation Conference*, Colorado Springs, CO, 27–30 June 2011.

26. Allik, B.; Ilg, M.; Zurakowski, R. Ballistic Roll Estimation Using EKF Frequency Tracking and Adaptive Noise Cancellation. *IEEE Transactions on Aerospace and Electronic Systems* **2013,** *49* (4), 2546–2553.

27. DeSpirito, J; Silton, S.; Weinacht, P.; Navier-Stokes Predictions of Dynamic Stability Derivatives: Evaluation of Steady-State Methods. *Journal of Spacecraft and Rockets* **2009,** *46* (6), 1142–1154.

28. Koren, A.; Idan, M.; Golan, O. Integrated Sliding Mode Guidance and Control for a Missile With On-Off Actuators. *Journal of Guidance, Control, and Dynamics* **2008,** *31* (1), 204–214.

29. Idan, M.; Shima, T.; Golan, O. Integrated Sliding Mode Autopilot-Guidance for Dual-Control Missiles. *Journal of Guidance, Control, and Dynamics* **2007,** *30* (4), 1081–1089.

30. Shima, T.; Idan, M.; Golan, O. Sliding-Mode Control for Integrated Missile Autopilot Guidance. *Journal of Guidance, Control, and Dynamics* **2006,** *29* (2), 250–260.

31. Iliff, K. Parameter Estimation for Flight Vehicles. *Journal of Guidance* **1989,** *12* (5), 609–622.

32. Klein, V.; Morelli, E. A. *Aircraft System Identification;* AIAA Education Series; American Institute of Aeronautics and Astronautics: Reston, VA, 2006.

33. Fresconi, F.; Celmins, I.; Silton, S. *Theory, Guidance, and Flight Control for High Maneuverability Projectiles;* ARL-TR-6767; U.S. Army Research Laboratory: Aberdeen Proving Ground, MD, 2014.

Nomenclature

D	=	diameter (m)
S	=	reference area (m^2)
m	=	mass (kg)
$\vec{I}$	=	moment of inertia tensor (kg-m^2)
$V, \vec{V}_{CG/I} = [u \quad v \quad w]^T$	=	total velocity of projectile, velocity of center of gravity with respect to inertial frame in body-fixed coordinates (m/s)
ρ	=	atmospheric density (kg/m^3)
q	=	dynamic pressure (N/m^2)
M	=	Mach number
$\alpha = asin\left[\dfrac{w}{\sqrt{u^2 + w^2}}\right]$	=	pitch angle of attack (rad)
$\beta = asin\left[\dfrac{v}{\sqrt{u^2 + v^2 + w^2}}\right]$	=	yaw angle of attack (rad)
$\bar{\alpha} = asin\left[\dfrac{\sqrt{v^2 + w^2}}{\sqrt{u^2 + v^2 + w^2}}\right]$	=	total angle of attack (rad)
$\phi_A = atan\left(\dfrac{v}{w}\right)$	=	aerodynamic roll angle (rad)
X, Y, Z	=	aerodynamic forces acting on projectile (N)
X_G, Y_G, Z_G	=	gravity forces acting on projectile (N)
L, M, N	=	aerodynamic moments acting on projectile (Nm)
$C_X, C_{X_0}, C_{X_{\bar{\alpha}^2}}$	=	total, zero-yaw, and yaw-dependent axial force coefficient
$C_N, C_{N_0}, C_{N_\alpha}, C_{N_{\alpha^3}}$	=	total, trim, linear and nonlinear normal force coefficient
C_{l_p}	=	roll damping moment coefficient
$C_m, C_{m_0}, C_{m_\alpha}, C_{m_{\alpha^3}}$	=	total, trim, linear and nonlinear pitching moment coefficient
C_{m_q}	=	pitch damping moment coefficient
$C_{Y_{p\alpha}}$	=	Magnus force coefficient
$C_{n_{p\alpha}}$	=	Magnus moment coefficient

$$x_{CP}, r_{CP} \quad = \quad \text{axial center of pressure, radial CP (m)}$$

$$\vec{r}_{CG \rightarrow CP_i} = \begin{bmatrix} x_{CP} & r_{CP} cos(\phi_{B_i}) & r_{CP} sin(\phi_{B_i}) \end{bmatrix}^T \quad = \quad \text{vector from center of gravity to ith moveable aerodynamic surface center of pressure (m)}$$

$$\phi_{CMD}, \phi_C, \phi_B, \Phi, \hat{\phi} \quad = \quad \text{Earth-fixed commanded, Earth-fixed control, body-fixed control, relative, and stowed roll angles (rad)}$$

$$\vec{T}_{BM_i} = \begin{bmatrix} 1 & 0 & 0 \\ 0 & cos(\Phi_i) & sin(\Phi_i) \\ 0 & -sin(\Phi_i) & cos(\Phi_i) \end{bmatrix} \quad = \quad \text{transformation matrix from body-fixed to moveable aerodynamic surface coordinates}$$

$$\vec{T}_{BE}$$
$$= \begin{bmatrix} c_\theta c_\psi & s_\phi s_\theta c_\psi - c_\phi s_\psi & c_\phi s_\theta c_\psi + s_\phi s_\psi \\ c_\theta s_\psi & s_\phi s_\theta s_\psi + c_\phi c_\psi & c_\phi s_\theta c_\psi + s_\phi s_\psi \\ -s_\theta & s_\phi c_\theta & c_\phi c_\theta \end{bmatrix} \quad = \quad \text{transformation matrix from body-fixed to Earth-fixed coordinates}$$

$$x, y, z \quad = \quad \text{inertial position (m)}$$

$$\dot{x}, \dot{y}, \dot{z} \quad = \quad \text{inertial translational velocity (m/s)}$$

$$\dot{u}, \dot{v}, \dot{w} \quad = \quad \text{time rate of change of body-fixed coordinate system translational velocity (m/s}^2\text{)}$$

$$\phi, \theta, \psi \quad = \quad \text{roll, pitch, and yaw Euler angles (rad)}$$

$$\dot{\phi}, \dot{\theta}, \dot{\psi} \quad = \quad \text{time rate of change of Euler angles (rad/s)}$$

$$\vec{\omega}_{B/I} = \begin{bmatrix} p & q & r \end{bmatrix}^T \quad = \quad \text{body-fixed coordinate system rotational velocity (rad/s)}$$

$$\dot{p}, \dot{q}, \dot{r} \quad = \quad \text{time rate of change of body-fixed coordinate system rotational velocity (rad/s}^2\text{)}$$

$$x_B, y_B, z_B \quad = \quad \text{body-fixed coordinate system}$$

$$x_E, y_E, z_E \quad = \quad \text{Earth-fixed coordinate system}$$

$$\vec{r}_{PT}^B, \vec{r}_{OT}^I, \vec{r}_{OP}^I \quad = \quad \text{vector from projectile to target, origin to target, and origin to projectile (m)}$$

$$\epsilon_y, \epsilon_z \quad = \quad \text{body-fixed coordinates of lateral components of vector from projectile to target in detector plane (m)}$$

$$\tilde{\epsilon}_y, \tilde{\epsilon}_z \quad = \quad \text{fixed-plane coordinates of lateral components of vector from projectile to target in detector plane (m)}$$

$$f_L \quad = \quad \text{lens focal length (m)}$$

$$\tilde{r}_z \quad = \quad \text{vertical reference fixed-plane coordinates (m)}$$

$\vec{y}, \vec{r}, \vec{e}, \vec{K}, \vec{u}, \vec{H}$	=	feedback measurement, reference, error, gain, control, and system dynamics matrices
$\vec{\theta}$	=	parameter vector
$\ddot{\varepsilon}, \dot{\varepsilon}, \varepsilon$	=	acceleration, velocity, and position for surrogate model
$\xi, \omega_n, f_\mu, \mu$		damping, natural frequency, control scaling, and control input of surrogate model
$\vec{A}_C$	=	controlled system dynamics matrix